1 **The influence of dynamics and emissions changes on China's wintertime haze**

2 Peter Sherman[1], Meng Gao[2], Shaojie Song[2], Patrick Ohiomoba[2], Alex Archibald[3,4], Michael

3 McElroy[1,2]

4 [1]Department of Earth and Planetary Sciences, Harvard University, Cambridge, Massachusetts

5 02138, United States

6 [2]School of Engineering and Applied Sciences, Harvard University, Cambridge, Massachusetts

7 02138, United States

8 [3]Department of Chemistry, University of Cambridge, Lensfield Road, Cambridge, UK

9 [4]National Centre for Atmospheric Science, UK

10 Corresponding author: Michael McElroy (mbm@seas.harvard.edu)

11

Abstract

13 Haze days induced by aerosol pollution in North and East China have posed a persistent and

14 growing problem over the past few decades. These events are particularly threatening to densely-

15 populated cities such as Beijing. While the sources of this pollution are predominantly

16 anthropogenic, natural climate variations may also play a role in allowing for atmospheric

17 conditions conducive to formation of severe haze episodes over populated areas. Here, an

18 investigation is conducted into the effects of changes in global dynamics and emissions on air

19 quality in China's polluted regions using 35 simulations developed from the Community Earth

20 Systems Model Large Ensemble (CESM LENS) run over the period 1920-2100. It is shown that

21 internal variability significantly modulates aerosol optical depth (AOD) over China; it takes

22 roughly a decade for the forced response to balance the effects from internal variability even in

23 China's most polluted regions. Random forest regressions are used to accurately model ($R^2 > 0.9$)

24 wintertime AOD using just climate oscillations, the month of the year and emissions. How

25 different phases of each oscillation affect aerosol loading are projected using these regressions.

26 AOD responses are identified for each oscillation, with particularly strong responses from El Niño-

27 Southern Oscillation (ENSO) and the Pacific Decadal Oscillation (PDO). As ENSO can be

28 projected a few months in advance and improvements in linear inverse modelling (LIM) may yield

29 a similar predictability for the PDO, results of this study offer opportunities to improve the

30 predictability of China's severe wintertime haze events, and to inform policy options that could

31 mitigate subsequent health impacts.

32

1. Introduction

Growth in China's population over the past several decades has coincided with a period of intense industrialization. This combination has precipitated a jumpstart in China's economy – which skyrocketed from the 10th largest economy in the world in 1980 to the second largest in 2018. Unfortunately, this has given rise also to serious public health issues induced by increased air pollution. According to the World Health Organization, 91% of the world's population lives in areas where air quality exceeds guideline limits (WHO 2016). Notably, air quality standards were met in only 84 of China's 338 prefecture-level cities in 2016 (China News Network 2017). The problem is especially pervasive in winter, when stable synoptic meteorological conditions can contribute to particularly strong haze events (Zheng et al. 2015). The Chinese government attempted to mitigate this issue by temporarily shutting down roughly 40% of its factories at the end of 2017 (more measures in Zheng et al. 2018). The rationale behind the decision is that coal consumption is one of the dominant sources of China's air pollution (Guan et al. 2016). While the sources over this region are primarily anthropogenic, the meteorological conditions that are conducive to stagnant weather are driven largely by natural causes. An important question is, what is the role of natural climate variability and how will it affect China's air quality in the future?

Teleconnection patterns refer to connections in climate anomalies over large spatial scales. They project as emergent patterns, and typically exhibit oscillatory behavior, with positive and negative phases corresponding to different atmospheric and oceanic phenomena. Teleconnections are caused by couplings of the atmospheric, oceanic, cryospheric and land-based processes, in what we refer to here interchangeably as natural variability and internal variability. One such example is the Arctic Oscillation (AO), where the positive phase reflects low surface pressure anomalies in

56 the north polar region and the negative shows the opposite (Higgins et al. 2000). The AO may be

57 connected to the high-pressure region of Mongolia, the Siberian High, a wintertime anticyclonic

58 pressure system over northeast Eurasia (Wu and Wang 2002; Gong et al. 2001). The strength and

59 position of the Siberian High are key modulators of the East Asian Winter Monsoon (Ding et al.

60 2014; Jia et al. 2015), which transports cool, clean air into China's heavily polluted regions,

61 clearing out aerosols which have accumulated over roughly a week (Yang et al. 2016). Since this

62 teleconnection may influence the Siberian High, changes in the AO could have important

63 implications for China's air quality.

64

65 Several studies have investigated potential connections between other oscillations and climate in

66 China (Mantua et al. 1997; Dima and Lohmann 2007; Zhang et al. 2007). Si and Ding (2016) found

67 that the Pacific Decadal Oscillation (PDO) and Atlantic Multidecadal Oscillation (AMO) are

68 important drivers of East Asian summer rainfall, and proposed a potential interaction between the

69 two oscillations through formation of a global stationary baroclinic wave train. Chen et al. (2013)

70 determined that the relationship between the winter and summer monsoons is associated

71 predominantly with El Niño-Southern Oscillation (ENSO) SST anomalies, with an anomalous

72 anticyclone over the western Pacific that persists from winter to spring during El Niño events.

73 They note a similar anticyclonic pattern during the positive phase of the PDO. As many have

74 suggested that these oscillations – particularly ENSO and the PDO – affect the monsoonal

75 circulation over East Asia there is reason to suspect that they could also have significant bearing

76 on China's air quality. Finding strong connections between the oscillations and air pollution would

77 facilitate better understanding of the underlying atmospheric mechanisms and could allow for

78 improved prediction of haze conditions. From a more general perspective, Kushnir et al. (2019)

79   note the importance of climate models for predicting extreme events given the sparsity of

80   observational data. Numerous studies have investigated the reverse scenario – the effect of

81   aerosols on teleconnections (Shindell et al. 2015; Shindell et al. 2009; Booth et al. 2012). The fact

82   that the aerosol-teleconnection interaction could be bidirectional is an important consideration for

83   prediction of both air quality changes and internal variability in the future.

84

85   Here, we analyze 35 simulations of wintertime (December-January-February) monthly 550 nm

86   aerosol optical depth (AOD) derived from the Community Earth Systems Model Large Ensemble

87   (CESM LENS; Kay et al. 2015) over the period 1920-2100 to assess how internal variability has

88   influenced China's wintertime haze (typically nitrate, sulfate, ammonium, organic aerosol and

89   black carbon) and how it could influence pollution in the future. We use AOD because it well

90   represents spatio-temporal changes in anthropogenic emissions, can be validated with MODIS

91   observations (Figure S1), and has been shown to correlate well with $PM_{2.5}$ in China (Xin et al.

92   2014). We then train random forest regressors to predict haze spatially over eastern China. We

93   exploit this model to project how changes in the oscillation indices could be reflected in China's

94   AOD.

95

96   **2. Method**

97   *2.1 Data overview – CESM LENS*

98   CESM LENS is an ensemble of 40 fully-coupled CESM1 simulations covering the period 1920-

99   2100. The model begins with a multicentury simulation of a year, 1850, selected as representative

100 of preindustrial conditions. The model, with constant forcing, reaches a quasi-equilibrium after a

101   few centuries. 1 January, year 402 of this simulation is taken to provide the initial conditions for

102   the first member of the ensemble which is run from 1850-1920 (Deser et al. 2012). This simulation

103   is integrated then to the year 2100, and is considered the first ensemble member. The remaining

104   39 simulations are initialized for the same year 1920, except for perturbations in initial air

105   temperatures (on the order of 10^{-14} K). These slight differences between simulations impact the

106   global climate system by altering internal variability. The consequences of this are reflected in

107   alterations of natural climate oscillation indices. Since we are investigating the impacts of specific

108   climate oscillation indices – some of which are calculated using SST data – we exclude five of the

109   40 simulations as they are run by a different climate modelling group, one at the University of

110   Toronto, and show systematic temperature biases relative to the rest of the ensemble. While

111   internal variability differs from simulation to simulation, external forcing is consistent for each

112   member of the ensemble: Coupled Model Intercomparison Projects version 5 (CMIP5) forcings

113   from 1920-2005 and the Representative Concentration Pathway with 8.5 Wm^{-2} of additional

114   radiative forcing (RCP8.5) from 2006-2100. This fact can be exploited to assess the strength of

115   external forcing changes relative to uncertainty associated with internal variability within CESM

116   LENS. Prior works have taken advantage of this fact to tease out the relative importance of internal

117   variability and the forced response (Deser et al. 2012; Vega-Westhoff and Sriver 2017). Further

118   elaboration of the ensemble is discussed in Kay et al. (2015).

119

120   The Community Atmosphere Model version 5 (CAM5; Conley et al. 2012) is the atmospheric

121   component of CESM LENS. Since we are investigating changes in aerosol optical depth (AOD)

122   within CESM LENS, we will narrow our discussion of CAM5 to its aerosol component. The

123   CAM5 model used in the CESM LENS simulations contains 30 vertical layers extending up to 3

124   hPa (roughly 30 km). It utilizes the simplified 3-mode modal aerosol scheme (MAM-3; Liu et al.

125   2012), which includes only Aitkin, accumulation and coarse aerosol modes. A number of

126   assumptions are made in this simplified scheme. For the purposes of this research the most

127   important assumption is that NH_3 is not simulated and ammonium is prescribed (Neale et al. 2012).

128   The interactive aerosols within this CAM5 scheme are black carbon, primary organic matter,

129   sulfate, dust, sea salt and secondary organic aerosol, which are included in calculating total AOD

130   over the visible spectrum, the response variable that we investigate in this study. CESM LENS

131   implements anthropogenic emissions from the Lamarque et al. (2010) IPCC AR5 emissions dataset

132   for 1920-2005 and emissions corresponding to RCP8.5 from 2006-2100.

133

134   *2.2 Comparing internal variability with the forced response*

135   To compare the forced response to internal variability inherent in the model, we compute the

136   timescale for each response. The forced response is simply the mean AOD of the 35 simulations

137   over each time step, and the timescale associated with this is associated with its temporal

138   derivative. The response due to internal variability is the standard deviation of the 35 models at

139   each time step. Comparing the mean ratio of these two time series shows how long it takes for the

140   forced response to balance internal variability. If the internal response is greater than the forced

141   response, we would expect natural variability to play an important role in modulating China's

142   wintertime AOD.

143

144   *2.3 Regression modelling and prediction*

145   Random forest regression is an ensemble machine learning technique that works by aggregating

146   decision tree models defined on subsamples of the feature space. Random forest regression

147   improves upon the decision tree method (a technique that is often used in weather prediction) by

148   aggregating over many decision trees to limit the risk of overfitting. In our analysis we use random

149   forest models composed of 100 decision trees with each tree calculating a regression based on

150   mean-squared loss in a randomly selected subset of the feature space. Our overall model is defined

151   on a feature space that includes ENSO, AMO, AO and PDO indices, months of the year and local

152   SOx (SO_2 + H_2SO_4) emissions as the input features and local AOD as the response. The spatially-

153   averaged winter (DJF) SOx emissions over all of China that are used in CESM LENS are shown

154   in Figure S2.

155

156   The oscillation indices are defined for each ensemble member through NCAR's Climate

157   Variability Diagnostics Package (Phillips et al. 2014). The AO index is defined by the first

158   Empirical Orthogonal Function (EOF) of sea level pressure. The AMO index is defined by the

159   detrended time series (i.e. with the effects of anthropogenic climate change removed) of North

160   Atlantic SSTs (Trenberth and Shea 2006). The ENSO index used here is NINO3.4, defined by

161   area-weighted sea surface temperature anomalies over a specific region of the tropical Pacific

162   (Wolter 1987). The PDO index is defined by the first EOF of the mean SST anomaly from

163   November to March over the Pacific Ocean north of 20°N (Zhang et al. 1997). As the AMO, ENSO

164   and PDO indices are calculated based on regional SSTs, we discuss briefly here the ocean

165   component of CESM LENS, Parallel Ocean Program, version 2 (POP2; Smith et al. 2010). POP2

166   is a three-dimensional ocean general circulation model, which, in this case, uses 60 vertical layers.

167   Given the lack of global oceanic observations in 1850, POP2 was initialized from a state of rest

168   based on modern observations, taking advantage of the fact that the upper ocean equilibrates with

169   the atmosphere on short timescales and that the long timescales associated with the deep ocean

170   mean that modern observations at depth are reflective also of preindustrial conditions. Once the

171   climate system reached a quasi-equilibrium in the multicentury 1850 run, the CESM LENS

172   simulation was run.

173

174   The spatial patterns of the oscillations are well represented by CESM LENS (Figure S3). We divide

175   China into grid cells and our overall model is composed of individual random forest regression

176   models for each grid cell. Each random forest model is trained on the same 70-30 train-test split

177   of the data. While independent regressions are run for each individual grid cell, the spatial

178   correlation structure is still accounted for because the oscillation data used as model inputs affect

179   the meteorology, which connects pollution in nearby locations. To investigate potential delayed

180   AOD responses to the natural oscillations, we added as inputs oscillation indices at 0 to 11 month

181   lags. In order to minimize computation time, we removed lags that did not contribute importantly

182   to the regression. Interactions between the different oscillations were accounted for in the feature

183   model by creating separate indices for the product of each oscillation pair. After training the model

184   at a given location, we predict AOD with the test set of inputs and compare to the actual CESM

185   LENS value at the corresponding location, using R^2 as an assessment of the model's predictive

186   power.

187

188   Once trained and tested, the random forest models can be used to predict the effects of individual

189   oscillations. To do this, we stochastically select percentile values for the oscillation indices for the

190   negative and positive phases of the individual oscillations. Given the structure of the oscillation

191   data, the negative phase of the oscillation is defined at approximately the 20th percentile and the

192   positive phase is defined at approximately the 80th percentile. Predicting AOD with these modified

193   oscillations in our overall model will provide AOD under negative and positive oscillation

194   conditions at each spatial coordinate. This method is performed for each oscillation and the AOD

195   differences between the positive and negative oscillations are used to assess how AOD changes

196   when going from a positive-phased oscillation to the negative complement – or vice versa.

197

198   **3. Results**

199   *3.1 Comparing internal variability with the forced response*

200   The timescales for the forced AOD response to balance internal AOD variability in China are

201   shown in Figure 1. Internal variability plays a significant role over the whole region and it takes at

202   least roughly a decade for it to be balanced by the forced response throughout China. From the

203   spatial distribution, it can be seen that the forced response is greatest in eastern China, which makes

204   sense because of the region's high levels of anthropogenic emissions. Despite this, it takes roughly

205   a decade for the effects of the forced response to balance internal variability even over eastern

206   China. We may conclude from Figure 1 that natural climate variability is important for China's

207   haze and it is thus crucial to assess the impacts that each oscillation might have on AOD.

208

209   *3.2 Regression modelling fit and predictions*

210   These effects are investigated in the random forest regressor. The R^2 fit is shown in Figure 2.

211   Strong fits ($R^2 > 0.9$) are seen over eastern China, where pollution levels are highest and have the

212   most important implications for human health. Notably, the fit is poorer in West China, where

213   temporally-averaged AOD is much smaller and exhibits a noisier response.

214

215   Percent AOD differences between the positive (80th percentile) and negative (20th) phases of the

216   major climate oscillations investigated are shown in Figure 3. The AOD distributions reveal that

217   the impacts due to changing ENSO and PDO phases are the most substantial, with AOD

218   differences of almost 10% as the climate system shifts from positive to negative phases of ENSO

219   and PDO. With ENSO, the largest AOD response takes place over south China, where AOD

220   increases during the positive phase (i.e. El Niño). Zhao et al. (2018) note a similar spatial pattern,

221   which they associate with an anomalous anticyclone that forms over the Philippine Sea during El

222   Niño responsible for transport of water vapor and aerosols to the region. With the AMO, there is

223   a moderate increasing AOD trend over the studied region during the positive AMO phase relative

224   to the negative. Wang et al. (2009) propose that a weakened winter land-sea temperature gradient

225   over Eurasia during AMO+ may induce weakened westerlies/anomalous easterlies that moderate

226   the transport mechanism removing pollution from the region. Therefore, this result also agrees

227   with previous research. With the AO, there is a slight anomalously negative AOD during its

228   positive phase over most of the region; however, the connection detected here, like the one for

229   AMO, is weak. With the PDO, a dipole response can be seen, with lower AOD in the north and

230   higher AOD in the south, corresponding likely to anomalous northerly winds during the positive

231   phase transporting pollution southward. This could be connected also to the similar ENSO pattern

232   seen here as proposed by Zhao et al. (2018).

233

234   *3.3 Physical explanations*

235   Now that potential connections between ENSO, AMO, AO and PDO indices and China's

236   wintertime AOD have been established from our regression models, we will discuss these effects

237   in terms of potential physical explanations. Figure 4 shows the composite difference in sea level

238   pressure (PSL) and 850 hPa winds between positive (80th percentile) and negative (20th) oscillation

239   phases. During El Niño, there is anomalously high pressure over the Philippine Sea, consistent

240   with the proposed anomalously high-pressure system responsible for the transport of water vapor

241   and aerosol into South China. Southwesterly winds are observed in this region during El Niño,

242   which also comply with this result. The ENSO PSL response is noted also by Li et al. (2017).

243   There is not a notable PSL response to the different AMO phases, but the winds tend to confine

244   local pollution over the region more during AMO+, which explains why more pollution is

245   predicted by the regression. The difference between AO phases shows a slight strengthening and

246   eastward shift of the Siberian High and a weakening of the Aleutian Low, which explains the

247   highly uncertain response pattern displayed in Figure 3. This result agrees with previous literature,

248   such as Wu and Wang (2002), who note that the AO and Siberian High are parts of a coupled

249   system where the AO can affect the Siberian High, but the relationship is not consistent over time.

250   It can also be seen in Figure 3 that the positive phase of the PDO has both a stronger Siberian High

251   and a deeper Aleutian Low relative to the negative phase, which increases the pressure gradient

252   contributing to a more powerful East Asian Winter Monsoon. This is reflected in the enhanced

253   westerly winds in North China during PDO+, which transport much of the heavily-polluted air

254   offshore. There is concurrently an anomalous anticyclone that forms over the Philippine Sea –

255   much like the El Niño response – explaining the north-south dipole response seen in AOD.

256

257   Temperature differences at 500 hPa for the four oscillations are displayed in Figure 5. South China

258   cools while the adjacent waters warm during El Niño, amplifying the winter land-sea temperature

259   gradient and encouraging stronger westerly winds that could enhance the anomalous anticyclone

260   formed over the region. There is a general warming over East Asia compared to the western Pacific

261   during AMO+, which weakens the land-sea temperature gradient and could explain why winds are

262   more westward in China during the positive phase. This agrees with Wang et al. (2009) who note

263   that land warming over Eurasia during AMO+ takes place in the mid and upper troposphere. The

264   AO reflects a similar temperature pattern as the AMO, albeit with more exaggerated trends, which

265   is realized in the presence of anomalous easterlies during the positive phase. Similarly, the PDO

266   composites match the general ENSO pattern with a cooler south China and warmer Pacific

267   encouraging the anomalous anticyclone.

268

269   **4. Discussion and Conclusions**

270   The main purpose of this study was to evaluate the relative importance of emissions and natural

271   climate variability on China's wintertime haze using the CESM LENS. This could allow for

272   refined prediction of severe haze events as the model allows a level of predictive granularity of up

273   to a few months in advance for the climate oscillations investigated here. We found that random

274   forest regressions form the basis of a framework that could be used to predict AOD with high

275   fidelity ($R^2 > 0.9$) over China's eastern half using as input parameters only climate oscillations,

276   the month of the year and emissions. The framework provides a means with which to assess the

277   country-wide contributions attributable to the oscillations and emissions. The results derived from

278   the regression are notably consistent with past findings and with meteorological changes observed

279   under changing oscillation states.

280

281   A large difference is seen in South China's pollution between the different ENSO phases, a result

282   that agrees with Zhao et al. (2018), who proposed a physical explanation involving formation of

283   an anomalous anticyclone over the Philippine Sea during El Niño resulting in transport of

284 additional water vapor and aerosols to the region, a suggestion supported by the present analysis.

285 We find also an increase in AOD during AMO+ relative to AMO−, which agrees with the AMO

286 theory proposed by Wang et al. (2009), in which higher Eurasian winter temperatures during

287 AMO+ are responsible for weakening the land-sea temperature gradient, providing impetus for

288 anomalous westward winds relative to AMO−. The effects from the AO are subject to large

289 variance, which limits our understanding of its effects (if any) on China's AOD. The PDO exhibits

290 a dipole response in AOD, with a decline in North China during the positive phase − connected

291 potentially to a weaker Siberian High-Aleutian Low pressure gradient − with an increase in South

292 China, connected to the anomalous anticyclone that forms during El Niño. The largest overall

293 effects are attributable to changing ENSO and PDO phases, with changes as large as 21.9% in

294 AOD for ENSO and 9.8% for PDO.

295

296 There are a number of limitations that should be noted for this study. First, we investigate here

297 internal variability and how it manifests itself in terms of a specific CESM ensemble. While we

298 have found physical explanations for the CESM LENS AOD variability that align with previous

299 studies, a next step in this research will be to employ a number of different general circulation

300 models imposing conditions that mirror positive and negative phases of the studied oscillations to

301 further validate the present results. We could also implement visibility data from meteorological

302 stations, where the longest datasets extend back to the 1950s. While this comparison could be

303 done, weak spatial coverage, along with missing data render these observations unhelpful for a

304 data problem that is already very noisy. Evaluation of observed AOD trends is difficult apart from

305 the most recent period (i.e. 2000-present), which is too limited of a historical scope to investigate

306 connections with oscillations whose phases can last for many decades. We have compared the

307   magnitude of CESM LENS AOD with AOD measurements from the MODIS instruments (Figure

308   S1). While CESM LENS underestimates the magnitude of AOD in China, it does capture the

309   general spatial structure as observed from MODIS – low AOD in western and central China, and

310   high AOD in southern and eastern China. The observational data are indicative of the reliability of

311   our results since the spatial structure compares favorably with that from CESM LENS. Another

312   limitation is the CESM LENS aerosol-chemistry scheme, which is simplified in both its mode

313   scheme and its treatment of NH_3 and ammonium. The scheme also limits our ability to accurately

314   represent anthropogenic emissions in our regression models, where we use only SOx emissions as

315   input and are unable to include NOx emissions. Given that SOx emissions also correlate

316   significantly with NOx, particulate organic matter and secondary organic aerosol emissions (not

317   shown), there is good reason to believe that SOx emissions should provide a good surrogate for

318   anthropogenic emissions, and this is reflected in the strong R^2 over East China. It is important to

319   note that China's haze formation involves complicated processes with many questions remaining

320   to be answered (e.g. Song et al. 2018). However, since this research is investigating dynamical

321   effects related to natural climate variability, issues associated with CAM5 chemistry should not

322   have significant bearing on our results.

323

328

329   **References**

330   Booth, B.B.B., Dunstone, N.J., Halloran, P.R., Andrews, T. and Bellouin, N., 2012: Aerosols

331   implicated as a prime driver of twentieth-century North Atlantic climate variability. *Nat.*,

332   **485**, 534–534, https://doi.org/10.1038/nature10946.

333   Chen, W., Feng, J., Wu, R., 2013: Roles of ENSO and PDO in the Link of the East Asian winter

334   monsoon to the following summer monsoon. *J. Climate,* **26**, 622–635,

335   https://doi.org/10.1175/JCLI-D-12-00021.1.

336   China News Network, 2017: In 2016, the ambient air quality of 84 cities nationwide increased by

337   11. Accessed 19 January 2019, http://www.chinanews.com/gn/2017/01-20/8131237.shtml.

338   Conley, A.J., and Coauthors, 2012: Description of the NCAR Community Atmosphere Model

339   (CAM 5.0). NCAR technical note.

340   Deser, C., Phillips, A., Bourdette, V., Teng, H., 2012: Uncertainty in climate change projections:

341   The role of internal variability. *Climate Dyn.,* **38**, 527–546,

342   https://doi.org/10.1007/s00382-010-0977-x.

343   Dima, M., and Lohmann, G., 2007: A hemispheric mechanism for the Atlantic multidecadal

344   oscillation, *J. Climate*, **20**, 2706-2719, https://doi.org/10.1175/JCLI4174.1.

345   Ding Y., Liu, Y., Liang, S., Ma, X.Q., Zhang, Y., Dong, S.Y., Liang, P., 2014: Interdecadal

346   variability of the East Asian winter monsoon and its possible links to global climate change.

347   *J. Meteor. Res.*, **28**, 693–713, https://doi.org/10.1007/s13351-014-4046-y.

348   Gong, D.Y., Wang, S.W., Zhu, J.H., 2001: East Asian winter monsoon and Arctic oscillation.

349   *Geophys. Res. Lett.*, **28**, 2073– 2076, https://doi.org/10.1029/2000GL012311.

350   Guan, W.J., Zheng, X.Y., Chung, K.F., Zhong, N.S. 2016: Impact of air pollution on the burden

351   of chronic respiratory diseases in China: time for urgent action. *Lancet*, **388**, 1939-1951,

352   https://doi.org/10.1016/S0140-6736(16)31597-5.

Accepted for publication in *Journal of Applied Meteorology and Climatology.* DOI 10.1175/JAMC-D-19-0035.1.

16

353   Higgins, R.W., Leetmaa, A., Xue, Y., Barnston, A., 2000: Dominant factors influencing the

354   seasonal predictability of U.S. precipitation and surface air temperature. *J. Climate*, **13**,

355   3994-4017, https://doi.org/10.1175/1520-0442(2000)013<3994:DFITSP>2.0.CO;2.

356   Jia, B., Wang, Y., Yao, Y., Xie, Y., 2015: A new indicator on the impact of large-scale circulation

357   on wintertime particulate matter pollution over China. *Atmos. Chem. Phys.*, **15**, 11919–

358   11929, https://doi.org/10.5194/acp-15-11919-2015.

359   Kay, J.E., and Coauthors, 2015: The Community Earth System Model (CESM) Large Ensemble

360   Project: A Community Resource for Studying Climate Change in the Presence of Internal

361   Climate Variability. *Bull. Amer. Meteor. Soc.*, **96**, 1333-1349,

362   https://doi.org/10.1175/BAMS-D-13-00255.1.

363   Kushnir, Y. and Coauthors, 2019: Towards operational predictions of the near-term climate. *Nat.*

364   *Clim. Change*. https://doi.org/10.1038/s41558-018-0359-7.

365   Lamarque, J.F., and Coauthors, 2010: Historical (18502000) gridded anthropogenic and biomass

366   burning emissions of reactive gases and aerosols: methodology and application. *Atmos.*

367   *Chem. Phys.*, **10**, 7017-7039, https://doi.org/10.5194/acp-10-7017-2010.

368   Li, T., Wang, B., Wu, B., Zhou, T., Chang, C.P, Zhang, R. 2017: Theories on Formation of an

369   Anomalous Anticyclone in Western North Pacific during El Niño: A review. *J. Meteor.*

370   *Res.*, **31**, 987-1006, https://doi.org/10.1007/s13351-017-7147-6.

371   Liu, X., and Coauthors, 2012: Toward a minimal representation of aerosols in climate models:

372   Description and evaluation in the Community Atmosphere Model CAM5. *Geosci. Model*

373   *Dev.*, **5**, 709–739, https://doi.org/10.5194/gmd-5-709-2012.

374   Mantua, N. J., Hare, S.R., Zhang, Y., Wallace, J.M., Francis, R.C., 1997: A Pacific interdecadal

375   climate oscillation with impacts on salmon production. *Bull. Amer. Meteor. Soc.*, **78**, 1069–

376   1079, https://doi.org/10.1175/1520-0477(1997)078<1069:APICOW>2.0.CO;2.

377   Neale, R.B., and Coauthors, 2012: Description of the NCAR Community Atmosphere Model

378   (CAM 5.0). Tech. Report NCAR/TN-486+STR.

379   Phillips, A.S., Deser, C., Fasullo, J., 2014: Evaluating modes of variability in climate

380   models. *EOS*, **95**, 453-455.

381   Shindell, D., and Faluvegi, G., 2009: Climate response to regional radiative forcing during the

382   twentieth century, *Nat. Geosci.*, **2**(4), 294–300, https://doi.org/10.1038/ngeo473.

383   Shindell, D.T., Faluvegi, G., Rotstayn, L. and Milly, G., 2015: Spatial patterns of radiative forcing

384   and surface temperature response, *J. Geophys. Res. Atmos.*, **120**, 5385–5403,

385   https://doi.org/10.1002/2014JD022752.

386   Si, D., and Ding, Y.H., 2016: Oceanic forcings of the interdecadal variability in East Asian summer

387   rainfall. *J. Climate*, **29**, 7633–7649, https://doi.org/10.1175/JCLI-D-15-0792.1.

388   Smith, R.D., and Coauthors, 2010: The Parallel Ocean Program (POP) reference manual. Los

389   Alamos National Laboratory Tech. Rep. LAUR-10-01853, 140.

390   Song, S., and Coauthors, 2018: Possible heterogeneous hydroxymethanesulfonate (HMS)

391   chemistry in northern China winter haze and implications for rapid sulfate formation.

392   *Atmos. Chem. Phys.*, 1-26, https://doi.org/10.5194/acp-2018-1015.

393   Trenberth, K.E. and Shea, D.J., 2006: Atlantic hurricanes and natural variability in 2005. *Geophys.*

394   *Res. Lett.*, **33**, L12704, https://doi.org/10.1029/2006GL026894.

395 Vega-Westhoff, B. and Sriver, R.L., 2017: Analysis of ENSO's response to unforced variability

396   and   anthropogenic   forcing   using   CESM. *Sci.   Rep.*, **7**,   18047,

397   https://doi.org/10.1038/s41598-017-18459-8.

398 Wang, Y.M., Li, S.L., Luo, D.H., 2009: Seasonal response of Asian monsoonal climate to the

399   Atlantic   multidecadal   oscillation.   *J.   Geophys.   Res.*, **114**,   D02112,

400   https://doi.org/10.1029/2008JD010929.

401 World Health Organization (WHO)., 2016: Ambient Air Pollution: A Global Assessment of

402   Exposure and Burden of Disease.

403 Wolter, K., 1987: The Southern Oscillation in surface circulation and climate over the tropical

404   Atlantic, Eastern Pacific, and Indian Oceans as captured by cluster analysis. *J. Clim. Appl.*

405   *Meteor.*,   **26**,   540-558,   https://doi.org/10.1175/1520-

406   0450(1987)026<0540:TSOISC>2.0.CO;2.

407 Wu, B., and Wang, J., 2002: Winter Arctic Oscillation, Siberian High and East Asian winter

408   monsoon. *Geophys. Res. Lett.*, **29**(19), 1897, https://doi.org/10.1029/2002GL015373.

409 Xin, J.Y., Zhang, Q., Wang, L.L., Gong, C.S., Wang, Y.S., Liu, Z.R., and Gao, W.K., 2014: The

410   empirical relationship between the PM2.5 concentration and aerosol optical depth over the

411   background of North China from 2009 to 2011. *Atmos. Res.*, **138**, 179–188.

412 Yang, Y., Liao, H., Lou, S., 2016: Increase in winter haze over eastern China in recent decades:

413   Roles of variations in meteorological parameters and anthropogenic emissions. *J. Geophys.*

414   *Res. Atmos.* **121**, 13050–13065, https://doi.org/10.1002/2016JD025136.

415 Zhang, Y., Wallace, J.M., Battisti, D.S., 1997: ENSO-like interdecadal variability: 1900-93. *J.*

416   *Climate*,   **10**,   1004-1020,   https://doi.org/10.1175/1520-

417   0442(1997)010<1004:ELIV>2.0.CO;2.

418   Zhang, R., Delworth, T.L., Held, I., 2007: Can the Atlantic Ocean drive the observed multidecadal

419   variability in Northern Hemisphere mean temperature? *Geophys. Res. Lett.*, **34**, L0270,

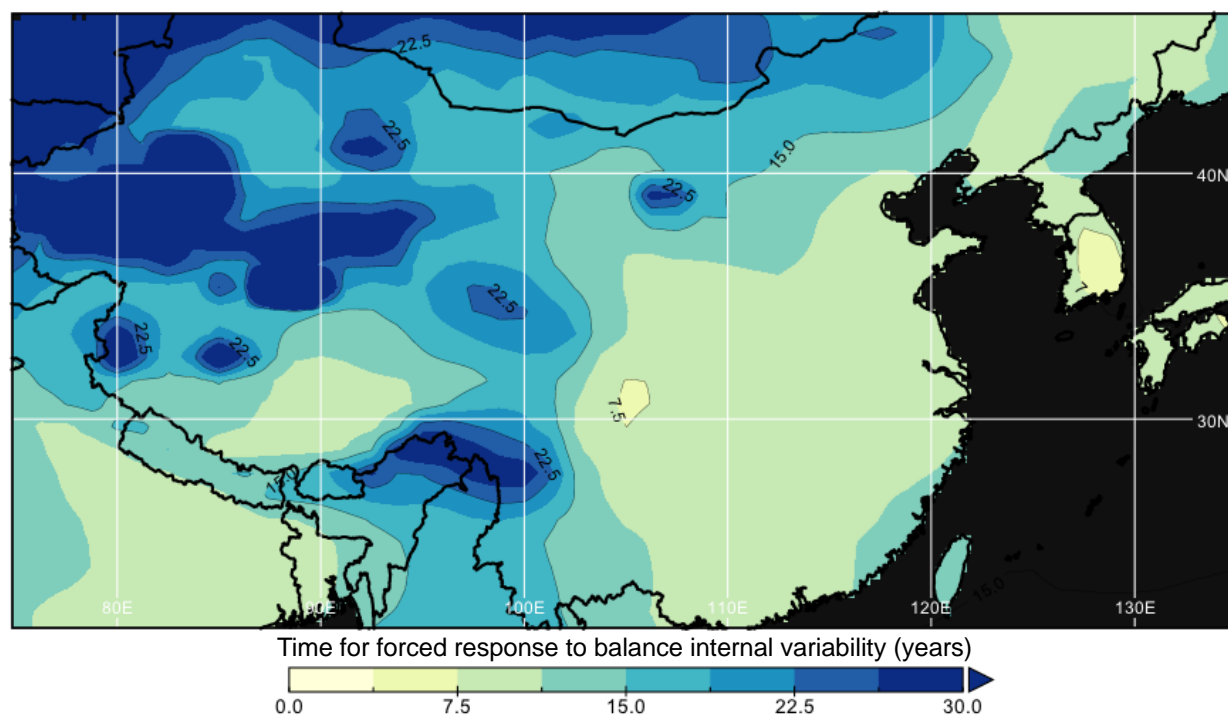420   https://doi.org/10.1029/2006GL028683.

421   Zhao S., Zhang, H., Xie, B. 2018: The effects of El Niño–Southern Oscillation on the winter haze

422   pollution of China. *Atmos. Chem. Phys.*, **18**, 1863–1877. https://doi.org/10.5194/acp-18-

423   1863-2018.

424   Zheng, B., and Coauthors, 2018: Trends in China's anthropogenic emissions since 2010 as the

425   consequence of clean air actions. *Atmos. Chem. Phys.*, **18**, 14095-14111,

426   https://doi.org/10.5194/acp-18-14095-2018.

427   Zheng, G.J., and Coauthors, 2015: Exploring the severe winter haze in Beijing: the impact of

428   synoptic weather, regional transport and heterogeneous reactions. *Atmos. Chem. Phys.* **15**,

429   2969-2983, https://doi.org/10.5194/acp-15-2969-2015.

430

Figures

Time for forced response to balance internal variability (years)

Figure 1. Timescale (in years) for the AOD forced response to balance the effects due to internal variability. This timescale is defined as the ratio of the ensemble AOD standard deviation to the ensemble AOD forced response (in years^{-1}). Contours are defined in terms of the major scale ticks denoted in the color bar. Data are masked out over the ocean.

Test set R^2

438
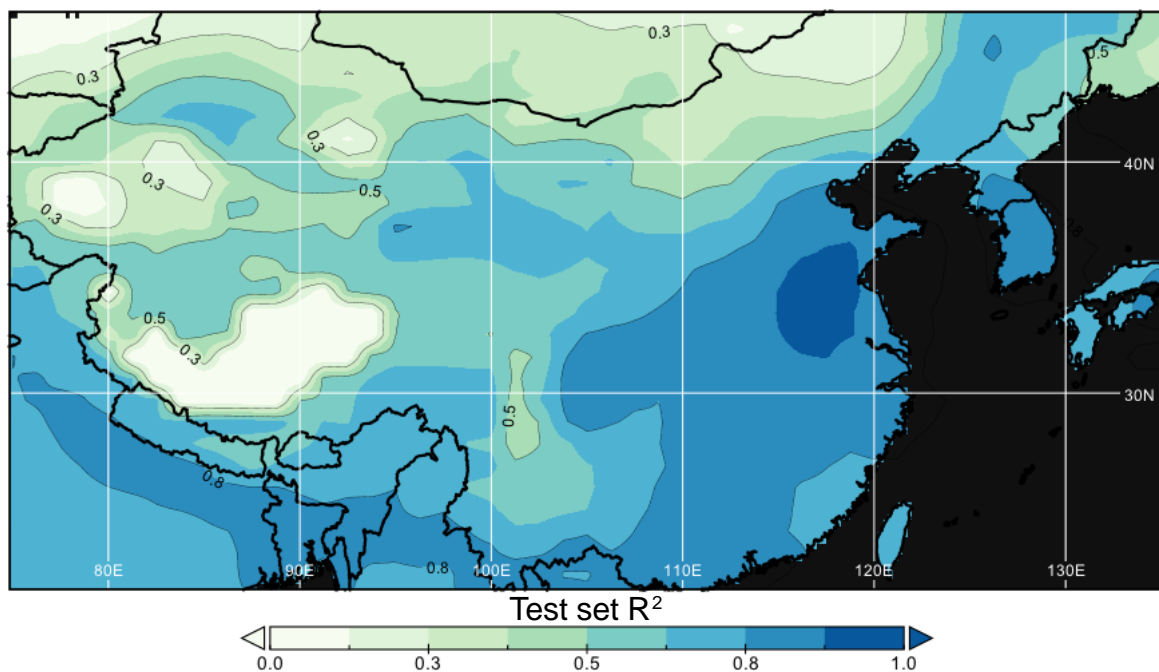
439   **Figure 2.** Spatial distributions of the test set R^2 for the random forest regressor fit to AOD for

440   each geographic location. Each regressor uses the oscillation indices, the month of the year and

441   local emissions as parameters with AOD as the response variable. Contours are defined in terms

442   of the major scale ticks denoted in the color bar. Data are masked out over the ocean.

443
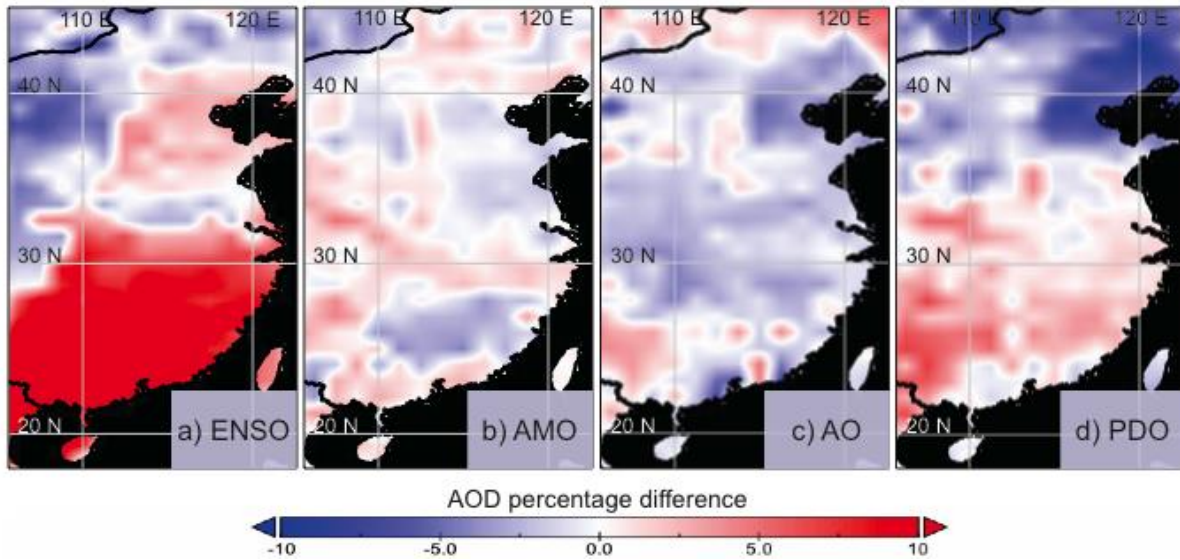
Figure 3. Random forest-derived projections of AOD percentage differences between (a) ENSO+ and ENSO–, (b) AMO+ and AMO–, (c) AO+ and AO– and (d) PDO+ and PDO–. Data are masked out over the ocean.

444

445

446

447

448
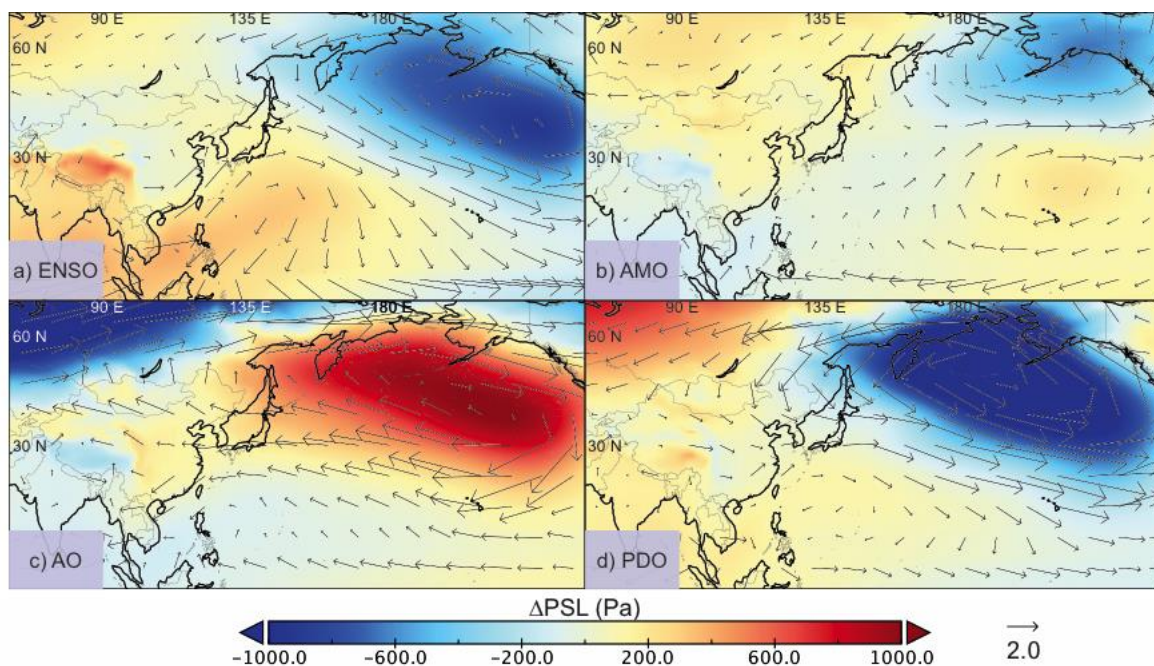
Figure 4. Composite differences in PSL for (a) ENSO+ and ENSO–, (b) AMO+ and AMO–, (c) AO+ and AO– and (d) PDO+ and PDO–. Composite differences of the 850 hPa winds are the overlaid as arrows on top of each subplot. The wind arrows are specified in units of ms^{-1} with a 2 ms^{-1} scale as indicated at the bottom of the figure.
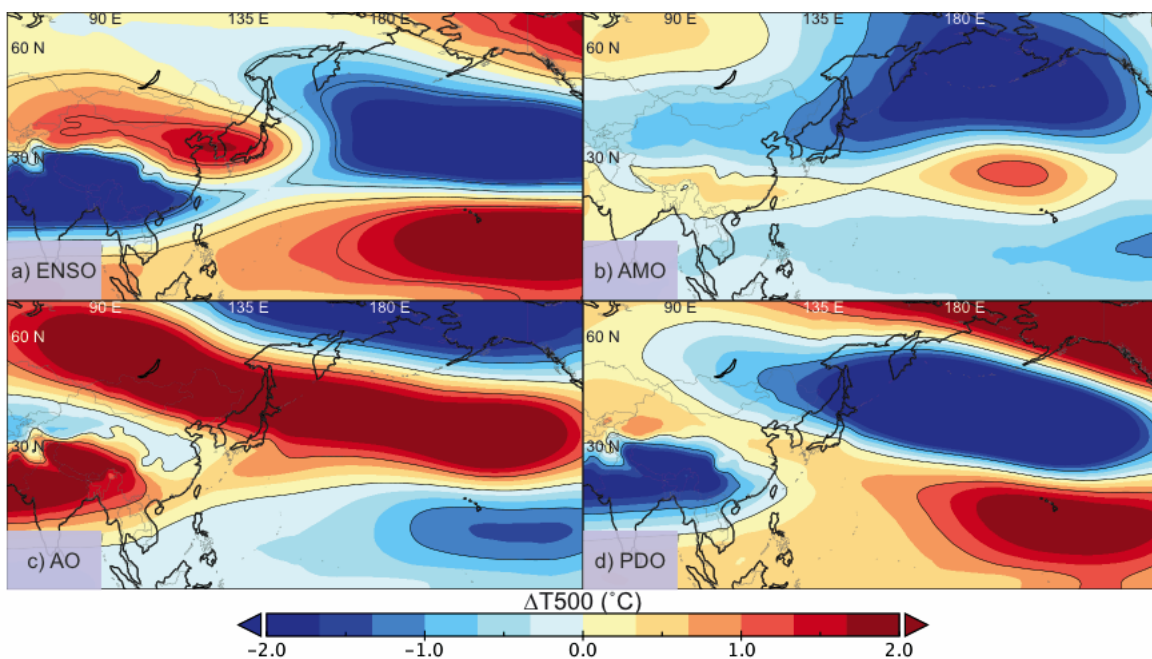
Figure 5. Same as Figure 4, but with T500.